Encapsulating Mobile Proton Carriers into Structural Defects in Coordination Polymer Crystals: High Anhydrous Proton Conduction and Fuel Cell Application

Munehiro Inukai,[†,‡] Satoshi Horike,*,[§] Tomoya Itakura,[∥] Ryota Shinozaki,[∥] Naoki Ogiwara,[§] Daiki Umeyama,[§] Sanjog Nagarkar,[†] Yusuke Nishiyama,[⊥,#] Michal Malon,[⊥,#] Akari Hayashi,[▽] Takashi Ohhara,[□,¶] Ryoji Kiyanagi,[□] and Susumu Kitagawa*,[†,§]

[†]Institute for Integrated Cell-Material Sciences (WPI-iCeMS), Kyoto University, Yoshida, Sakyo-ku, Kyoto 606-8501, Japan

[‡]Graduate School of Science and Technology, Tokushima University, 2-1 minami-Josanjima-Cho, Tokushima 770-8506, Japan

[§]Department of Synthetic Chemistry and Biological Chemistry, Graduate School of Engineering, Kyoto University, Katsura, Nishikyo-ku, Kyoto 615-8510, Japan

[∥]DENSO Corporation, 1-1, Showa-cho, Kariya, Aichi 448-8661, Japan

[⊥]JEOL Resonance Inc., 3-1-2 Musashino, Akishima, Tokyo 196-8558, Japan

[#]RIKEN CLST-JEOL Collaboration Center, Yokohama, Kanagawa 230-0045, Japan

[▽]International Research Center for Hydrogen Energy, Kyushu University, 744 Motooka, Nishi-ku, Fukuoka 819-0395, Japan

[□]J-PARC Center, Japan Atomic Energy Agency, Tokai, Naka-gun 319-1195, Japan

[¶]Research Center for Neutron Science and Technology, Comprehensive Research Organization for Science and Society, Tokai, Ibaraki 319-1106, Japan

S *Supporting Information*

ABSTRACT: We describe the encapsulation of mobile proton carriers into defect sites in nonporous coordination polymers (CPs). The proton carriers were encapsulated with high mobility and provided high proton conductivity at 150 °C under anhydrous conditions. The high proton conductivity and nonporous nature of the CP allowed its application as an electrolyte in a fuel cell. The defects and mobile proton carriers were investigated using solid-state NMR, XAFS, XRD, and ICP-AES/EA. On the basis of these analyses, we concluded that the defect sites provide space for mobile uncoordinated H_3PO_4, $H_2PO_4^-$, and H_2O. These mobile carriers play a key role in expanding the proton-hopping path and promoting the mobility of protons in the coordination framework, leading to high proton conductivity and fuel cell power generation.
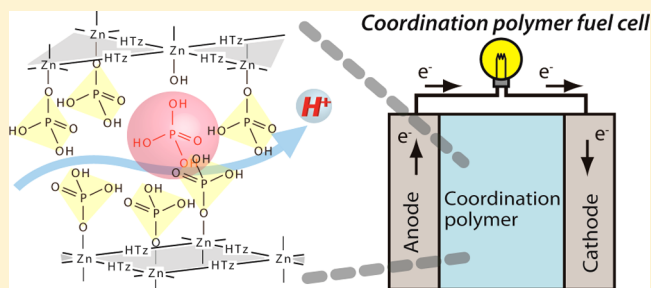
INTRODUCTION

The design of fast proton conductive solids for use at high temperature (100−200 °C) is of interest to materials chemistry from the viewpoint of fuel cell technology.[1] A powerful method to obtain high proton conductivity is to incorporate fast mobile proton carriers, which act as proton acceptor and donor sites, into proton conductive solids. For example, water in perfluorosulfonic acid polymers (e.g., Nafion) significantly promote proton conduction. However, such proton carriers migrate from the polymer chains at temperatures above 100 °C, resulting in low proton conduction.[2] Therefore, the development of proton conductive solids that strongly encapsulate proton carriers with high mobility is a challenge that requires addressing.[2c]

Porous coordination polymers (PCPs) and metal organic frameworks (MOFs) comprising metal ions and bridging ligands[3] have received attention as solid-state proton conductors because of their regular and designable pore structures and thermal stability.[4] Mobile proton carriers such as water,[5] amine,[6] and acid molecules[7] contained in the pores impart proton conductivity to PCPs and MOFs. Although many reported proton conductive PCPs and MOFs show high conductivity (above 10^{-3} S cm^{-1}),[7a,b,8] there is no report on the application of these materials as solid electrolytes for fuel cell devices. This is because of the drawbacks inherent to these materials, including the leaching of proton carriers from the pores and the fuel crossover problems due to their inherent porosity.[9] The former problem makes it difficult to maintain high proton conductivity of membrane electrode assemblies
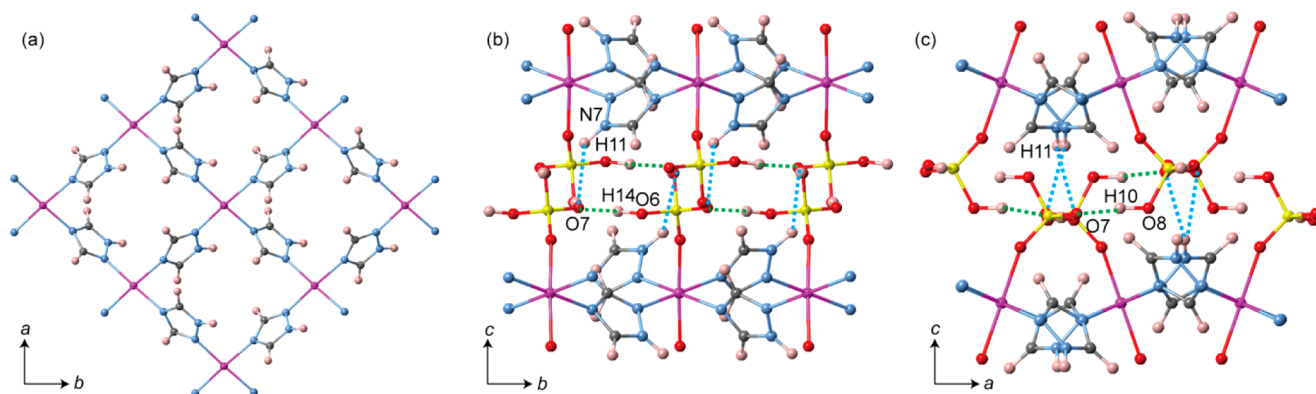
Figure 1. (a) Crystal structure of $[Zn(H_2PO_4)_2(C_2N_3H_3)_2]_n$ (**1s**) along the *c* axis at 290 K. $H_2PO_4^-$ groups are not shown to highlight the 2-D coordination framework. The hydrogen bonding (H-bonding) network of **1s** viewed from the (b) *a* and (c) *b* axis. H-bonds between adjacent $H_2PO_4^-$ ions, and between $H_2PO_4^-$ ions and HTz molecules, are shown as green and blue dotted lines, respectively. [Color coding: purple: Zn, yellow: P, red: O, blue: N, black: C, and light pink: H.].

(MEAs), which are a key architecture for fuel cell, and the latter problem causes a reduction in the electromotive force of the fuel cell. To overcome these problems and to apply these metal−organic hybrid materials to fuel cell devices, we have focused on the defects in nonporous coordination polymers (CPs) and present a strategy to both strongly encapsulate proton carriers with high mobility and avoid fuel crossover. Introduction of defects has recently been developed for PCPs/MOFs to modulate functions such as gas adsorption,[10] catalytic activity,[11] and proton conductivity;[12] however, defects in nonporous CPs have been less studied.

In this work, we propose a concept to make use of the defect sites in CP crystals for doping of proton carriers. The trapped carriers are maintained in the structure up to its decomposition temperature (ca. 180 °C). Consequently, we observed fast anhydrous proton conduction and successfully performed first demonstration of power generation using a fuel cell with the CP as the electrolyte.

■ RESULTS AND DISCUSSION

We employed a two-dimensional CP [Zn-$(H_2PO_4)_2(C_2N_3H_3)_2]_n$ (**1**),[13] which shows proton conduction under anhydrous conditions at 150 °C. Our previous study showed that protons mainly transport between the monodentate $H_2PO_4^-$ ions. To enhance the conductivity by incorporating proton carriers, more detailed information regarding proton conduction, including the location of the protons and the hopping pathway, is required. We first prepared a large single crystal of **1** (**1s**, 2.0 × 2.0 × 0.4 mm³) and analyzed the location of protons by single crystal neutron diffraction measurement at 290 K. **1s** is constructed from stacked two-dimensional (2-D) sheets comprising Zn^{2+}, 1,2,4-triazole (HTz), and $H_2PO_4^-$, i.e., [Zn-$(H_2PO_4)_2(C_2N_3H_3)_2]_n$ (Figure 1a). Two hydrogen atoms are present on the monodentate $H_2PO_4^-$, and three hydrogen atoms are present on the bidentate HTz. Protons H10 and H14 are connected to the proton donor sites O8 and O6 and point to the proton acceptor oxygen O7 of the inter- and intralayer $H_2PO_4^-$ ions. These distances are 1.01 Å (O8−H10), 1.55 Å (H10−O7), 1.01 Å (O6−H14), and 1.56 Å (H14−O7) (Figure 1b and 1c). These values are similar to those in other well-known proton conductors.[14] The distance H11−O7 between the HTz moiety and $H_2PO_4^-$ is 2.52 Å. Recent DFT calculations indicated that the typical intermolecular NH−O

distance capable of proton transport is ca. 1.3−1.7 Å.[15] The HTz protons do not contribute to proton hopping in the 2-D coordination frameworks. Our previous study suggested the reorientation of $H_2PO_4^-$ using ^2H solid-state NMR. H10 and H14 diffuse through 2-D proton transport pathways comprising rotative $H_2PO_4^-$ ions along the *ab* plane.

Synthesis of CPs with Proton Carriers Embedded in the Defects. Neutron diffraction analysis confirms that only monodentate $H_2PO_4^-$ plays a role in proton hopping. In general, the key strategies for enhancing conductivity are expanding the proton hopping pathway, increasing the concentration of protons, and improving the mobility of protons by doping with proton carriers.[2f] We addressed the introduction of defects to the monodentate $H_2PO_4^-$ network and the embedding of uncoordinated H_3PO_4, which has rotational and translational mobility. We reacted ZnO (2.0 mmol), HTz (4.0 mmol), and excess phosphoric acid solution in water by a liquid-assisted mechanochemical method. The amounts of the H_3PO_4 reacted were 4.0 (**2**, stoichiometric ratio), 4.4 (**3**), 4.8 (**4**), and 5.2 mmol (**5**). The solvent used for the assist was different from that used for **1** (ethanol) in our previous work[13] used to introduce monodentate $H_2PO_4^-$ defects.

We elucidated the ratio of elements using inductively coupled plasma atomic emission spectroscopy (ICP-AES) for Zn and P, and elemental analyses (EA) for C and N. The combination of ICP-AES and EA indicates a ratio of 1:1.6:4.1:5.8 (Zn:P:C:N) for **2** (Table 1). Compared to the ratio of defect free model, the ratio of P decreases from 2 to 1.6, whereas the ratios of C and N are similar to those of defect free model. This indicates the defect of monodentate $H_2PO_4^-$ coordinated to Zn^{2+}. In the case of **5**, the ratio of P is close to that of defect-free model, as are the ratios of C and N. This is due to the presence of uncoordinated H_3PO_4 in the defects of

Table 1. Elemental Analyses Using a Combination of ICP-AES and EA[a]

compound	Zn	P	C	N
defect-free model	1	2	4	6
2	1	1.6	4.1	5.8
5	1	1.8	4.0	5.6

[a]ICP-AES elucidated the ratios of Zn and P, and EA elucidated the ratios of C and N.

the monodentate $H_2PO_4^-$ framework (Figure 2). We also confirmed the ratio of Zn and P of single crystal sample (**1s**)
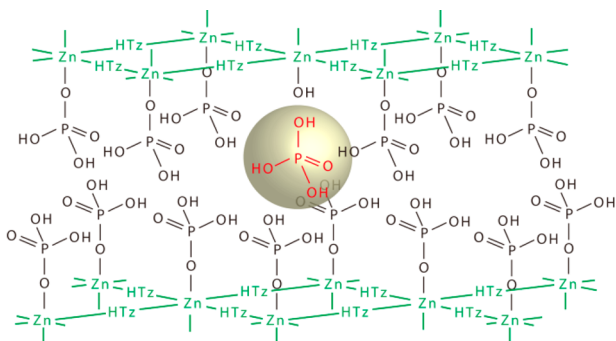
Figure 2. Proposed structural model of **5**. OH$^-$ is coordinated to Zn instead of monodentate $H_2PO_4^-$, whereas the uncoordinated H_3PO_4 occupies the space where the monodentate $H_2PO_4^-$ existed.

using ICP-AES. The ICP-AES indicates a ratio of 1:2.1 (Zn:P) for **1s**, suggesting few inherent defects of Zn^{2+} in the crystal. This result supports the defect of the powder compounds and the quantitative analysis of the defects. The results of X-ray diffraction (XRD), X-ray absorption fine structure (XAFS), and solid-state NMR measurement also support this model.

To confirm the crystal structures, we performed powder XRD measurements. The patterns show no extra peaks attributed to ZnO and HTz. All peak positions are similar to those of the original material **1**, indicating that its crystal structure is maintained (Figure 3a). However, the pattern of **2** shows a small additional peak at 10.5° (Figure 3b). This suggests that the part of the crystal structure around the defects changes slightly. In addition, the intensities of some peaks related to the coordination 2D sheets of [Zn−HTz]$^{2+}$ gradually increase with increasing ratio of reacted H_3PO_4 (Figure S2, Supporting Information). For example, the peak at 22.9° indicating the [004] plane gradually increases (Figure 3c). This would suggest improvement of crystallinity upon embedding H_3PO_4 into the defects. To confirm the thermal stability of the crystal structure, we performed variable temperature powder XRD measurements of compound **5**. The XRD patterns in 30−150 °C did not change, suggesting that the crystal structure of **5** was intact up to 150 °C even though the structure has defective sites.

To confirm the homogeneous distribution of H_3PO_4 in the particles, we performed scanning electron microscope energy-dispersive X-ray spectroscopy on cross-sections of particles of **5** (Figure S1, Supporting Information). EDX element mappings for Zn and P show homogeneous distributions of the elements, confirming the homogeneous distribution of H_3PO_4 in the particle. Thermogravimetric analysis (TGA) profiles indicate thermal stability up to ca. 180 °C, which is similar to the decomposition temperature of the original **1** (Figure S5, Supporting Information). The embedded H_3PO_4 is maintained in the 2-D coordination frameworks up to the decomposition temperature.

Proton Conductivity. The proton conductivities were obtained by AC impedance measurement under dry N_2 flow. Figure 4 shows Arrhenius plots for the proton conductivities of **2−5** from 30 °C to 150 °C under anhydrous conditions. The proton conductivities increase over the whole temperature range with increasing ratio of reacted H_3PO_4. Activation energies are 0.85, 0.57, 0.52, and 0.53 eV for **2**, **3**, **4**, and **5**,
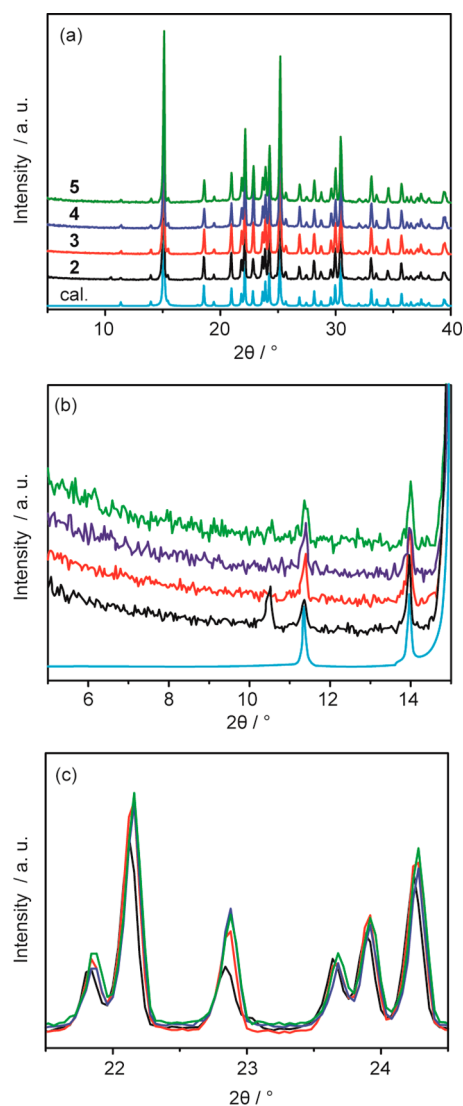
Figure 3. (a) XRD patterns: Calculated (light blue), **2** (black), **3** (red), **4** (blue), and **5** (green). The XRD patterns in the range of (b) 5−15° and (c) 21−25°. The calculation pattern is omitted in (c).
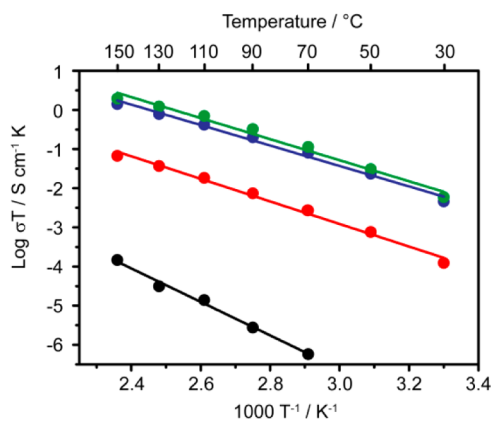

Figure 4. Arrhenius plot of conductivities of **2** (black circle), **3** (red circle), **4** (blue circle), and **5** (green circle) under dry N_2 flow.

respectively. Embedding H_3PO_4 significantly decreases the activation energy, while the effect is saturated in **4** and **5**. At 30 °C, the conductivity of **5** is enhanced to 0.02 mS cm^{-1}. The

proton conductivity of **5** reaches 4.6 mS cm^{-1} at 150 °C, which is ca. 10 000 times higher than that of **2**. The conductivity is among the highest reported for proton conductors, including PCPs and MOFs,[4] acid-doped polymers,[2f] and solid acids,[2b] at intermediate temperatures (100−200 °C) under anhydrous conditions. We also obtained time-dependence data for the conductivity at 150 °C to confirm the thermal stability of the conductivity. The observed conductivity is consistent for more than 900 min (Figure S6, Supporting Information). This high stability is due to robust encapsulation of H_3PO_4 into the defects.

H_2/O_2 Coordination Polymer Fuel Cell. The obtained proton conductivity is close to acceptable values (≥ca. 10 mS) for use as a fuel cell electrolyte.[2b] We prepared a H_2/O_2 fuel cell comprising **5** as an electrolyte and measured the current−voltage and current-power curve at 120 °C. The maximum open circuit voltage (OCV) is 0.88 V and is maintained for 1 h (Figure 5a), indicating little gas crossover and unfavorable
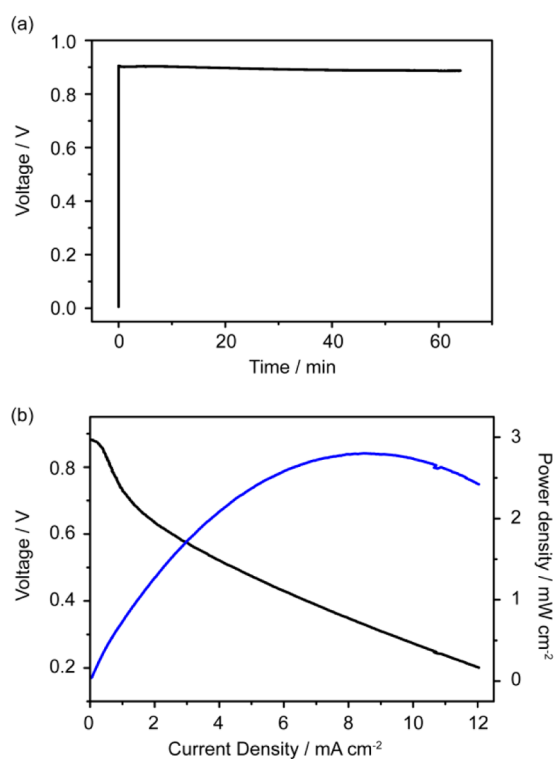

Figure 5. (a) Open circuit voltage in a H_2/O_2 fuel cell at 120 °C under anhydrous conditions. (b) Performance of H_2/O_2 fuel cell with **5** as the electrolyte at a relative humidity of 26% and 120 °C. Black and blue lines represent current−voltage and current−power, respectively.

chemical reactions. Compared to conventional porous crystalline solids, such as PCPs and MOFs, nonporous CPs are suitable materials for fuel cell electrolytes in terms of the gas crossover problem. Although the OCV value is slightly lower than the theoretical maximum of 1.16 V, it is comparable to that of conventional polymer electrolyte fuel cells.[16,1d] The maximum power density is 2.8 mW cm^{-2}. This is the first demonstration of power generation by a fuel cell with CPs/MOFs as the electrolyte. Compared to similar materials, the power density is higher than that of recently reported supramolecular metallogel proton conductors.[17] Although the obtained power density is lower than that of well-known fuel cells, including oxoacid- and phosphoric acid-doped poly-

mers,[1d] the power density could be improved by optimization of the electrode contact with the CP electrolyte, the thickness of the electrolyte, and the interface between the electrolyte and the electrode.

Observation of the Defects and the Mobile Proton Carriers. The embedded H_3PO_4 in the coordination polymers improves proton conductivity and allows the material to be applied in fuel cells. To monitor the local coordination environment of Zn^{2+}, we performed XAFS for **2** and **5**. Figure 6 shows the radial distribution functions (RDFs) derived from
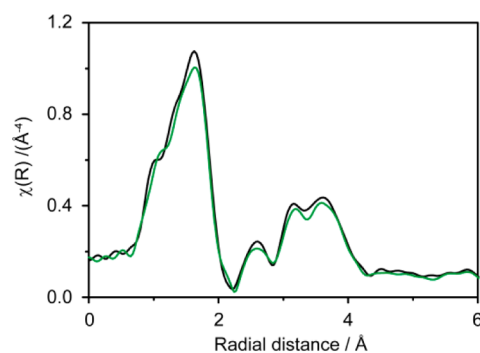

Figure 6. RDFs from Zn K-edge EXAFS spectra of **2** (black) and **5** (green) at room temperature.

extended X-ray absorption fin structure (EXAFS). In both patterns, a peak at 1.6 Å assigned to the first coordination sphere (Zn−O or Zn−N) appears.[18] The shape of the RDF for **2** is almost coincident with that of **5**. This indicates that no clear change in the first coordination structure is caused by excess phosphoric acid. XAFS analysis suggests that the Zn^{2+} first coordination sphere of **2** and **5** is Zn−O or Zn−N, whereas the combination of ICP-AES and EA indicates the defects in the monodentate $H_2PO_4^-$ framework in **2**. On the basis of the synthetic scheme, XRD, XAFS, ICP-AES, and EA, we assume that OH$^-$ is coordinated to Zn^{2+} instead of $H_2PO_4^-$. The above analyses fully support the proposed structural model (Figure 2).

To confirm the structural model, we investigated the structural defects in the monodentate $H_2PO_4^-$ framework and the existence of uncoordinated H_3PO_4 using ^{31}P solid-state magic angle spinning NMR with and without cross-polarization between ^1H and ^{31}P (CP-MAS NMR and MAS NMR). The CP-MAS NMR spectra reflect only the phosphorus of the framework and filter out NMR signals attributed to liquid-like highly mobile phosphorus. All the spectra show peaks at −3.2 and −5.7 ppm (Figure 7a). The existence of two peaks indicates that two types of monodentate $H_2PO_4^-$ exist in the framework; however, there is only one form of phosphorus present in the crystal structure, i.e., that attributed to monodentate $H_2PO_4^-$. The $^{31}P−^{31}P$ double quantum/single quantum (DQ/SQ) correlation spectrum, as shown in Figure 7c, shows distance correlation peaks between the two different peaks, suggesting both forms of $H_2PO_4^-$ are located within 1 nm of each other and are distributed homogeneously in the crystal structure. Thus, the peak at −3.2 ppm may be assigned to the phosphorus of $H_2PO_4^-$ near the coordinated OH$^-$. Thus, the two different peaks indicate the presence of defects in the monodentate $H_2PO_4^-$ framework.

The ^{31}P MAS NMR spectra for **4** and **5** show an additional large peak at 0.0 ppm and a small peak at −11.4 ppm (Figure 7b). A recent ^{31}P MAS NMR study revealed that the ^{31}P NMR
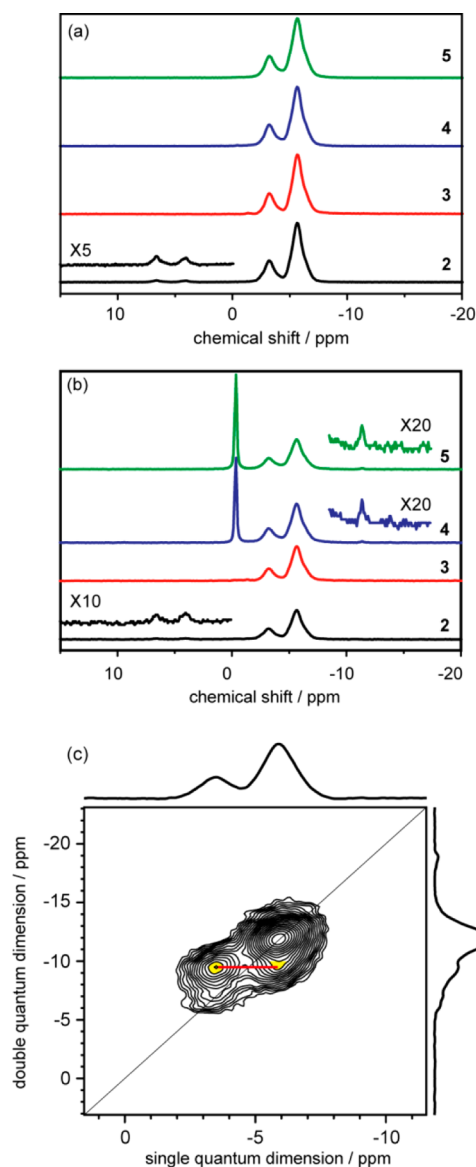
**Figure 7.** (a) ^{31}P CP-MAS NMR and (b) MAS NMR spectra for **2**, **3**, **4**, and **5** at room temperature. (c) DQ/SQ spectrum of **2** at room temperature. The red line connects the two correlation peaks highlighted in yellow.

defects in the framework are similar, even when H_3PO_4 is embedded into the crystal.

Proton Dynamics. The dynamics of the protons directly affect the proton conductivity. To study the effect of mobile H_3PO_4 and $H_2PO_4^-$ on the dynamics of the protons, we performed ultrafast MAS ^{1}H solid-state NMR measurement for **2** and **5**. Ultrafast MAS provides high-resolution ^{1}H NMR spectra of solid powder samples[20] and is an established tool used to reveal local structures and proton dynamics.[21] In the high-resolution ^{1}H NMR spectra (Figure 8a and 8b), **2** shows
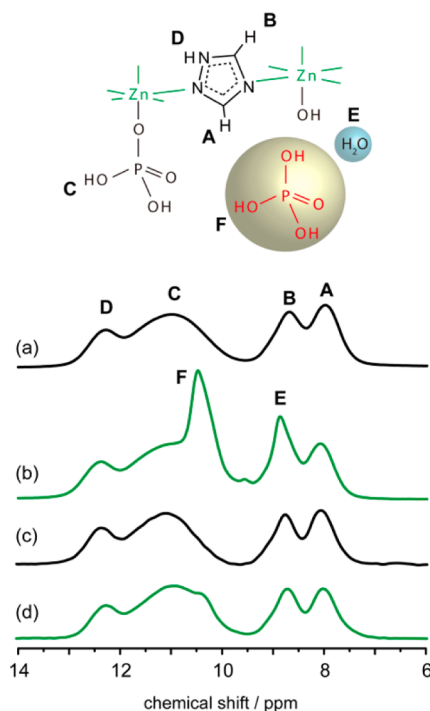
Figure 8. ^{1}H ultrafast MAS NMR spectra for (a) **2** (black line) and (b) **5** (green line) at room temperature. ^{1}H DQNMR spectra for (c) **2** (black line) and (d) **5** (green line) at room temperature.

spectrum of polybenzimidazole doped with phosphoric acid shows peaks at 0.5 and −12 ppm assigned to doped H_3PO_4 and $H_2PO_4^-$, respectively.[19] This suggests that the peaks at 0.0 and −11.4 ppm can be assigned to uncoordinated H_3PO_4 and $H_2PO_4^-$, respectively. The two peaks only appear in the MAS NMR spectra, which suggests that the coordination polymers contain both mobile uncoordinated H_3PO_4 and $H_2PO_4^-$. The anionic uncoordinated $H_2PO_4^-$ acts as a mobile proton donor site, provides a new proton hopping path, and lowers the activation energy. For the charge compensation for the uncoordinated $H_2PO_4^-$, a part of monodentate $H_2PO_4^-$ may change HPO_4^{2-}. **2** exhibits additional peaks at 4.0 and 6.5 ppm. In a similar way to the XRD analysis, this indicates a slight change in the structure of the crystal around the defects in **2**. Conversely, the intensities of the peaks at −3.2 and −5.7 ppm do not change, which is similar to the spectra of the CP-MAS. This indicates that the monodentate $H_2PO_4^-$ and the structural

clear peaks at 8.0, 8.7, 11.0, and 12.3 ppm. For the assignment for these peaks, we carried out ^{1}H−^{31}P double cross-polarization (double CP), ^{1}H−^{14}N heteronuclear multiple quantum coherence (HMQC), and 2-D ^{1}H−^{1}H double quantum filter (2-D DQNMR) measurement (Figures S8 and S9, Supporting Information). These spectra indicate that the peaks at 11.0 and 12.3 ppm are due to the two protons of monodentate $H_2PO_4^-$ and one proton of HTz (N−H). The other two peaks at 8.0 and 8.7 ppm are assigned to the remaining two protons of HTz (C−H). Peaks assigned to coordinated OH$^-$ may overlap around 11 ppm. In the spectra of **5**, new peaks appear at 8.9 and 10.5 ppm.

For assignment, we performed ^{1}H−^{1}H double quantum NMR (DQNMR), which highlights low mobility or static protons.[22] Figure 8c and 8d shows the DQNMR spectra for **2** and **5** at room temperature. In the spectrum of **5**, the additional peaks at 8.9 and 10.5 ppm in the MAS spectra of **5** disappear and the spectra shape becomes similar to those of the MAS and DQNMR spectra for **2**. The ^{31}P MAS studies indicate the presence of uncoordinated mobile H_3PO_4 and $H_2PO_4^-$. On the basis of the ^{31}P MAS NMR and ^{1}H DQNMR, the additional peaks at 8.9 and 10.5 ppm are assigned to the protons of mobile uncoordinated H_2O, and H_3PO_4 and $H_2PO_4^-$, respectively.

We also measured the ^{1}H spin−lattice relaxation time (T_{1H}) for **2** and **5** to discern whether the mobile species utilize all the protons in the H-bonds network. Table S1, Supporting Information, shows the T_{1H} values for **2** and **5**. All the T_{1H} values for **5** are smaller than those of **2**. This indicates that the mobile H_3PO_4, $H_2PO_4^-$, and H_2O create a new proton hopping pathway, including the mobile carriers and HTz, and promote the mobility of all protons from the monodentate $H_2PO_4^-$ and HTz. This is the main reason for the enhancement of proton conductivity and decrease in activation energy.

CONCLUSIONS

We presented a strategy to utilize defect sites in nonporous CP crystal to encapsulate proton carriers. The mobile proton carriers were maintained in the defects up to the decomposition temperature of the CPs and promoted the mobility of all protons in the CP, leading to stable high conductivity. In addition to the high conductivity, the nonporous nature provided a current−voltage curve without fuel crossover in the fuel cell. This is the first demonstration of power generation by a fuel cell in which CPs and MOFs were used as the electrolyte. To our knowledge, there have been very few reports of highly proton conductive crystalline solids that encapsulate mobile proton carriers into the structural defects of their crystal structures. Our strategy may be applied to other proton conductive crystalline solids, such as MOFs, metalphosphates, and oxoacids (e.g., $CsHSO_4$). We believe that this work will contribute to the development of proton conductive solids and further the application of CPs and MOFs to fuel cells.

ASSOCIATED CONTENT

Ⓢ Supporting Information

The Supporting Information is available free of charge on the ACS Publications website at DOI: 10.1021/jacs.6b03625.

> Experimental details, SEM-EDX images, TG profiles, time dependence of conductivity, solid-state NMR spectra, and T_{1H} (PDF)
> CIF data for **1s** at 77 K (CIF)
> CIF data for **1s** at 290 K (CIF)

AUTHOR INFORMATION

Corresponding Authors

*horike@sbchem.kyoto-u.ac.jp
*kitagawa@icems.kyoto-u.ac.jp

Author Contributions

The manuscript was written through contributions of all authors.

Notes

The authors declare no competing financial interest.

ACKNOWLEDGMENTS

REFERENCES

(1) (a) Li, Q.; He, R.; Jensen, J. O.; Bjerrum, N. J. *Chem. Mater.* **2003**, *15*, 4896−4915. (b) Wang, Y.; Chen, K. S.; Mishler, J.; Cho, S. C.; Adroher, X. C. *Appl. Energy* **2011**, *88*, 981−1007. (c) Zhang, H.; Shen, P. K. *Chem. Soc. Rev.* **2012**, *41*, 2382−2394. (d) Chandan, A.; Hattenberger, M.; El-kharouf, A.; Du, S.; Dhir, A.; Self, V.; Pollet, B. G.; Ingram, A.; Bujalski, W. *J. Power Sources* **2013**, *231*, 264−278.

(2) (a) Alberti, G.; Casciola, M. *Solid State Ionics* **2001**, *145*, 3−16. (b) Hogarth, W. H. J.; Diniz da Costa, J. C.; Lu, G. Q. *J. Power Sources* **2005**, *142*, 223−237. (c) Asensio, J. A.; Sánchez, E. M.; Gómez-Romero, P. *Chem. Soc. Rev.* **2010**, *39*, 3210−3239. (d) Bose, S.; Kuila, T.; Nguyen, T. X. H.; Kim, N. H.; Lau, K.-t.; Lee, J. H. *Prog. Polym. Sci.* **2011**, *36*, 813−843. (e) Laberty-Robert, C.; Vallé, K.; Pereira, F.; Sanchez, C. *Chem. Soc. Rev.* **2011**, *40*, 961−1005. (f) Zhang, H.; Shen, P. K. *Chem. Rev.* **2012**, *112*, 2780−2832.

(3) (a) Yaghi, O. M.; O'Keeffe, M.; Ockwig, N. W.; Chae, H. K.; Eddaoudi, M.; Kim, J. *Nature* **2003**, *423*, 705−714. (b) Kitagawa, S.; Kitaura, R.; Noro, S.-i. *Angew. Chem., Int. Ed.* **2004**, *43*, 2334−2375. (c) Ferey, G. *Chem. Soc. Rev.* **2008**, *37*, 191−214.

(4) (a) Horike, S.; Umeyama, D.; Kitagawa, S. *Acc. Chem. Res.* **2013**, *46*, 2376−2384. (b) Yamada, T.; Otsubo, K.; Makiura, R.; Kitagawa, H. *Chem. Soc. Rev.* **2013**, *42*, 6655−6669. (c) Yoon, M.; Suh, K.; Natarajan, S.; Kim, K. *Angew. Chem., Int. Ed.* **2013**, *52*, 2688−2700. (d) Ramaswamy, P.; Wong, N. E.; Shimizu, G. K. H. *Chem. Soc. Rev.* **2014**, *43*, 5913−5932.

(5) (a) Kitagawa, H.; Nagao, Y.; Fujishima, M.; Ikeda, R.; Kanda, S. *Inorg. Chem. Commun.* **2003**, *6*, 346−348. (b) Sahoo, S. C.; Kundu, T.; Banerjee, R. *J. Am. Chem. Soc.* **2011**, *133*, 17950−17958. (c) Jeong, N. C.; Samanta, B.; Lee, C. Y.; Farha, O. K.; Hupp, J. T. *J. Am. Chem. Soc.* **2012**, *134*, 51−54. (d) Taylor, J. M.; Dawson, K. W.; Shimizu, G. K. H. *J. Am. Chem. Soc.* **2013**, *135*, 1193−1196.

(6) (a) Bureekaew, S.; Horike, S.; Higuchi, M.; Mizuno, M.; Kawamura, T.; Tanaka, D.; Yanai, N.; Kitagawa, S. *Nat. Mater.* **2009**, *8*, 831−836. (b) Hurd, J. A.; Vaidhyanathan, R.; Thangadurai, V.; Ratcliffe, C. I.; Moudrakovski, I. L.; Shimizu, G. K. H. *Nat. Chem.* **2009**, *1*, 705−710. (c) Umeyama, D.; Horike, S.; Inukai, M.; Hijikata, Y.; Kitagawa, S. *Angew. Chem., Int. Ed.* **2011**, *50*, 11706−11709.

(7) (a) Sadakiyo, M.; Yamada, T.; Kitagawa, H. *J. Am. Chem. Soc.* **2009**, *131*, 9906−9907. (b) Ponomareva, V. G.; Kovalenko, K. A.; Chupakhin, A. P.; Dybtsev, D. N.; Shutova, E. S.; Fedin, V. P. *J. Am. Chem. Soc.* **2012**, *134*, 15640−15643.

(8) (a) Ohkoshi, S.-i.; Nakagawa, K.; Tomono, K.; Imoto, K.; Tsunobuchi, Y.; Tokoro, H. *J. Am. Chem. Soc.* **2010**, *132*, 6620−6621. (b) Panda, T.; Kundu, T.; Banerjee, R. *Chem. Commun.* **2012**, *48*, 5464−5466. (c) Umeyama, D.; Horike, S.; Inukai, M.; Kitagawa, S. *J. Am. Chem. Soc.* **2013**, *135*, 11345−50. (d) Bazaga-García, M.; Colodrero, R. M. P.; Papadaki, M.; Garczarek, P.; Zoń, J.; Olivera-Pastor, P.; Losilla, E. R.; León-Reina, L.; Aranda, M. A. G.; Choquesillo-Lazarte, D.; Demadis, K. D.; Cabeza, A. *J. Am. Chem. Soc.* **2014**, *136*, 5731−5739. (e) Nagarkar, S. S.; Unni, S. M.; Sharma, A.; Kurungot, S.; Ghosh, S. K. *Angew. Chem., Int. Ed.* **2014**, *53*, 2638−2642. (f) Nguyen, N. T. T.; Furukawa, H.; Gándara, F.; Trickett, C. A.; Jeong, H. M.; Cordova, K. E.; Yaghi, O. M. *J. Am. Chem. Soc.* **2015**, *137*, 15394−15397. (g) Phang, W. J.; Jo, H.; Lee, W. R.; Song, J. H.; Yoo, K.; Kim, B.; Hong, C. S. *Angew. Chem., Int. Ed.* **2015**, *54*, 5142−5146. (h) Ramaswamy, P.; Wong, N. E.; Gelfand, B. S.; Shimizu, G. K. H. *J. Am. Chem. Soc.* **2015**, *137*, 7640−7643.

(9) Kitagawa, H. *Nat. Chem.* **2009**, *1*, 689−690.

(10) Wu, H.; Chua, Y. S.; Krungleviciute, V.; Tyagi, M.; Chen, P.; Yildirim, T.; Zhou, W. *J. Am. Chem. Soc.* **2013**, *135*, 10525−32.

(11) (a) Ravon, U.; Savonnet, M.; Aguado, S.; Domine, M. E.; Janneau, E.; Farrusseng, D. *Microporous Mesoporous Mater.* **2010**, *129*, 319−329. (b) Park, T.-H.; Hickman, A. J.; Koh, K.; Martin, S.; Wong-Foy, A. G.; Sanford, M. S.; Matzger, A. J. *J. Am. Chem. Soc.* **2011**, *133*, 20138−20141. (c) Vermoortele, F.; Ameloot, R.; Alaerts, L.; Matthessen, R.; Carlier, B.; Fernandez, E. V. R.; Gascon, J.;

Kapteijn, F.; De Vos, D. E. *J. Mater. Chem.* **2012**, *22*, 10313−10321. (d) Ameloot, R.; Vermoortele, F.; Hofkens, J.; De Schryver, F. C.; De Vos, D. E.; Roeffaers, M. B. *Angew. Chem., Int. Ed.* **2013**, *52*, 401−5.

(12) Taylor, J. M.; Dekura, S.; Ikeda, R.; Kitagawa, H. *Chem. Mater.* **2015**, *27*, 2286−2289.

(13) Umeyama, D.; Horike, S.; Inukai, M.; Itakura, T.; Kitagawa, S. *J. Am. Chem. Soc.* **2012**, *134*, 12780−5.

(14) Kreuer, K.-D. *Chem. Mater.* **1996**, *8*, 610−641.

(15) (a) Zhang, D.; Yan, L. *J. Phys. Chem. B* **2010**, *114*, 12234−12241. (b) Yue, B.; Yan, L.; Han, S.; Xie, L. *J. Phys. Chem. B* **2013**, *117*, 7941−7949.

(16) Verma, A.; Scott, K. *J. Solid State Electrochem.* **2010**, *14*, 213−219.

(17) Aiyappa, H. B.; Saha, S.; Wadge, P.; Banerjee, R.; Kurungot, S. *Chem. Sci.* **2015**, *6*, 603−607.

(18) Umeyama, D.; Horike, S.; Inukai, M.; Itakura, T.; Kitagawa, S. *J. Am. Chem. Soc.* **2015**, *137*, 864−870.

(19) Hughes, C. E.; Haufe, S.; Angerstein, B.; Kalim, R.; Mähr, U.; Reiche, A.; Baldus, M. *J. Phys. Chem. B* **2004**, *108*, 13626−13631.

(20) (a) Nishiyama, Y.; Endo, Y.; Nemoto, T.; Utsumi, H.; Yamauchi, K.; Hioka, K.; Asakura, T. *J. Magn. Reson.* **2011**, *208*, 44−48. (b) Brown, S. P. *Solid State Nucl. Magn. Reson.* **2012**, *41*, 1−27.

(21) (a) Lee, Y. J.; Bingöl, B.; Murakhtina, T.; Sebastiani, D.; Meyer, W. H.; Wegner, G.; Spiess, H. W. *J. Phys. Chem. B* **2007**, *111*, 9711−9721. (b) Graf, R. *Solid State Nucl. Magn. Reson.* **2011**, *40*, 127−133.

(22) (a) Goward, G. R.; Schuster, M. F. H.; Sebastiani, D.; Schnell, I.; Spiess, H. W. *J. Phys. Chem. B* **2002**, *106*, 9322−9334. (b) Benhabbour, S. R.; Chapman, R. P.; Scharfenberger, G.; Meyer, W. H.; Goward, G. R. *Chem. Mater.* **2005**, *17*, 1605−1612.